Nanostructured Conductive Metal Organic Frameworks for Sustainable Low Charge Overpotentials in Li-Air Batteries

Leily Majidi[1], Alireza Ahmadiparidari[1], Nannan Shan[2], Sachin Kumar Singh[1], Zhehao Huang[3], Sina Rastegar[1], Khagesh Kumar[4], Zahra Hemmat[1], Anh T. Ngo[2,5], Peter Zapol[2], Jordi Cabana[4], Arunkumar Subramanian[1], Larry A. Curtiss[2&], Amin Salehi-Khojin[1&]

[1] Department of Mechanical and Industrial Engineering, University of Illinois at Chicago, Chicago, IL, 60607, USA.
[2] Materials Science Division, Argonne National Laboratory, Lemont, IL 60439, USA.
[3] Department of Materials and Environmental Chemistry, Stockholm University, Stockholm, 10691, Sweden.
[4] Department of Chemistry, University of Illinois at Chicago, Chicago, IL, 60607, USA.
[5] Department of Chemical Engineering, University of Illinois at Chicago, Chicago, IL, 60607, USA.

[&]Corresponding authors: salehikh@uic.edu, curtiss@anl.gov

Lithium-oxygen batteries are among the most attractive alternatives for the future electrified transportation. However, the practical application of these batteries is hindered by many obstacles. Due to insulating nature of Li_2O_2 product and the slow kinetics of reactions, attaining sustainable low charge overpotentials at high rates becomes a major challenge resulting in battery's early failure and low round trip efficiency. Herein, we discovered outstanding characteristics of a conductive metal organic framework (c-MOF) that promotes the growth of nanocrystalline Li_2O_2 products with amorphous regions. This provides a novel platform for the continuous growth of Li_2O_2 units away from framework enabling a fast discharge at high current rates. Moreover, the Li_2O_2 structure works in an excellent synergy with the redox mediator (RM) in the electrolyte. The conductivity of the amorphous Li_2O_2 structure allows the RM to act directly on the Li_2O_2 surface instead of catalyst edges and then transport through the electrolyte to the Li_2O_2 surface. This direct charge transfer enables a small charge potential of <3.7 V under high current densities (1-2 A/g) sustained for a long cycle life (100-300 cycles) for large capacities (1000-2000 mAh/g). These results open a new direction for utilizing c-MOFs towards advanced energy storage systems.

The development of beyond Li-ion batteries is critical to meet the future global demand for energy storage. Among beyond Li-ion batteries, lithium-oxygen (Li-O_2) battery is the most promising solution since it offers the highest theoretical energy density, that can substantially outperform Li-ion batteries[1–6]. Recently, Li-O_2 batteries have attracted a significant attention in various applications such as electrified transportation and smart grid systems; however, on the path of their practical use, there still remain many obstacles. The sluggish kinetics of the governing reactions during discharge and charge impose high overpotentials that result in low round trip efficiency[7,8]. Moreover, an inefficient decomposition of solid discharge products (Li_2O_2) and its accumulation on the surface of the cathode lead to poor cycling (early failure) in these systems[9,10].

To address these issues, discovery of new cathode materials with outstanding functionalities is essential. In this context, metal organic frameworks (MOFs) are promising platforms owing to their high porosity, large surface area, highly ordered structure and tunable chemical composition. These characteristics make MOFs an ideal candidate to be investigated as electrode materials in electrochemical energy applications[11–13] and especially rechargeable batteries[14–16]. However,

traditional MOFs are still far from practical cathode materials due to their insulating nature stemming from the redox-inactive organic ligands and low-energy electron transfer pathways[15,17–19]. Therefore, various design strategies have been employed to synthesize conductive MOFs (c-MOFs) with enhanced electron transport properties and structural stability crucial to advanced electrochemical systems[17,19–21]. While MOFs and MOF-based electrodes have been investigated in a number of Li-O$_2$ batteries[22,23,32,24–31], the performance of c-MOFs has remained unexplored. Herein, we report the first demonstration of a cathode based on a c-MOF, namely copper tetrahydroxyquinone (Cu-THQ), in a Li-O$_2$ battery system that operates without any conductive additive and with dry air. The Cu-THQ cathode works in synergy with an electrolyte combination comprised of a lithium nitrate (LiNO$_3$) salt and a bifunctional indium bromide (InBr$_3$) additive in a tetraethylene glycol dimethyl ether (TEGDME) solvent.

The previously synthesized bulk Cu-THQ[33] was exfoliated into 2D nanoflakes (NFs) via a liquid-phase exfoliation technique[34] (see Supporting Information S1). The electrical conductivity of synthesized Cu-THQ was reported to be ~1.5 × 10^{-7} S cm^{-1} at room temperature[33]. To prepare the c-MOF-based cathode, the exfoliated Cu-THQ NFs were then coated on a gas diffusion electrode (GDE) (see Experimental Section). Dynamic light scattering (DLS) results show an average size of 145 nm for the c-MOF flakes (Figure 1a). A survey by X-ray photoelectron spectroscopy (XPS) performed on the GDEs coated with Cu-THQ NFs is shown in Figure 1b, which confirms the presence of Cu, C and O on the cathode. The observed peaks for N and F in the spectrum are due to the synthesis process[33] and the polytetrafluoroethylene (PTFE) present on the GDE substrate[35], respectively. The obtained XPS results for Cu 2p and O 1s spectra are presented in Supporting Information S2. To assess the structural stability of c-MOF NFs after exfoliation, high-resolution transmission electron microscopy (HRTEM) images were acquired (see Supporting Information S3). The HRTEM images (Figure 1c-e) clearly show the open pores, smaller than 1 nm with a honeycomb arrangement along [001] with d_{110} = 1.13 nm and d_{020} = 1.10 nm, which agrees well with the AB stacking model of Cu-THQ (calculated d_{110} = 11.2 Å and d_{020} = 10.8 Å)[33]. These observations confirm that the crystal structure of Cu-THQ was preserved after exfoliation.

Cyclic voltammetry was performed using the Cu-THQ catalyst loaded on GDE to examine the catalytic activity of Cu-THQ in a three-electrode cell (Supporting Information S4). The battery cycling experiments were performed in a dry air environment with a custom-made Swagelok

battery setup assembled in an argon-filled glovebox. Li chips and Cu-THQ NFs coated on GDE were used as the anode and cathode, respectively. The electrolyte is comprised of a TEGDME solvent, 0.1M $InBr_3$ additive and 1M $LiNO_3$ salt. The concentration of 0.1 M $InBr_3$ was found to be effective in both increasing the cycle life and surpassing the charge overpotential (Supporting Information S5).

To evaluate the battery performance of this system, first a constant current density of 1 A/g was applied within a potential range of 2.5-4.0 V vs. Li/Li^+ under two limiting capacities of 1000 mAh/g (0.1 mAh/cm^2) and 2000 mAh/g (0.2 mAh/cm^2) (all capacity and current density values are reported per weight of the Cu-THQ catalyst). Supporting Figure S3 shows the battery results with 1000 mAh/g capacity operated up to 300 cycles, with a potential gap of 1.09 V at the 300th cycle. Figure 1f shows the charge-discharge profiles for the battery with the increased capacity of 2000 mAh/g and current density of 1 A/g. The battery cycling was stopped after 150 cycles when the discharge potential reached the 2.5 V cut-off voltage. A potential gap of 0.92 V was observed at the first cycle, which remained stable, with only a slight increase reaching 1.0 V at the end of cycling. We note that a discharge plateau at the 2nd cycle appears that is associated with the reduction of remaining Br_3^- (from the previous charge process) to Br^-[36,37]. At higher cycles, the plateau fades away with a similar trend observed in $Li-O_2$ battery cycling using $InBr_3$ and LiBr[36,37]. Figure 1g shows the results obtained under 2000 mAh/g limiting capacity and doubled current density of 2 A/g. This battery operates for 100 cycles before reaching the discharge cut-off potential. Under this condition, the potential gap increased from 1 V at the 1st cycle to 1.31 V at the 100th cycle. Considering the significantly high current density and extended capacity values, the charge profiles remain stable throughout the cycling of these batteries with a low charge potential of <3.7 V. More $Li-O_2$ battery control experiments results are shown in Supporting Information S5.

Figure 1h summarizes the variation of charge-discharge potential gap versus cycle life for different current densities and limiting capacity conditions. A rate capability experiment was also performed on the Cu-THQ cathode with a current density range of 0.25-2 A/g. The result shown in Figure 1i demonstrates the reversible discharge performance of battery under different rates tested up to 3500 mAh/g specific capacity.

Various characterization techniques were utilized to investigate possible changes in the cathode under cycling and to study the discharge products, the surface morphology of the cathode was

4

studied using scanning electron microscopy (SEM) after the 10th discharge and the consecutive charge process as shown in Figure 2a. The film-like structure of the product formed during discharge disappears at the end of the charge process (inset of Figure 2a) due to its decomposition. Differential electrochemical spectroscopy (DEMS) experiments were performed on the battery in order to quantitatively analyze the gas products during charge and discharge (see Figure 2b and Supporting Information S6). The calculated number of electrons per O_2 molecules consumed and evolved during discharge and charge processes are 2.06 and 2.03, respectively. These results confirm that Li_2O_2 is the only product, which reversibly forms and decomposes during the battery cycling. Moreover, no trace of CO_2 and water was detected after the charge process. To further characterize the cathode, XPS was performed after the 10th discharge. Figure 2c shows the main observed peaks of Li 1s and O 1s regions located at ~55.0 eV and ~531.7 eV, respectively, consistent with previously reported XPS results for Li_2O_2 formation[2,38].

The microstructure and composition of the cathode reaction product after its 10th discharge was analyzed using transmission electron microscopy (TEM). In this analysis, a cathode flake was suspended over a holey region within a TEM grid (Figure 2d). A high-resolution TEM (HR-TEM) micrograph acquired from this sample shows that the Li_2O_2 product attached to the Cu-THQ catalyst is comprised of 2-5 nm sized nanocrystalline grains embedded in amorphous Li_2O_2. Some of these crystalline Li_2O_2 particles are highlighted in Figure 2e and the indexed version of the fast Fourier transform (FFT) pattern in inset of this figure can be found in Supporting Figure S7a. The presence of Li_2O_2 on the edges of the Cu-THQ flake was further studied by performing electron energy loss spectroscopy (EELS) on the discharged cathode. The Cu-THQ flake used in this analysis is shown in Supporting Figure S7b and was suspended in the holey region of TEM grid in order to avoid interference from the carbon film below. The EELS spectra were acquired from two different locations (S1 and S2, which are marked in the micrograph of Supporting Figure S7b) at the edges of the discharged product and are presented in Figure 2f. The O K-edge spectrum is consistent with previously reported EELS data for Li_2O_2[39], which also accounted for the sharpest features at the Li K-edge.

Furthermore, X-ray diffraction (XRD) was performed on the pristine and cycled cathode after the 10th discharge (see Supporting Information S8). As shown in Supporting Figure S9, the persistence of Cu-THQ diffraction peaks on the discharged cathode confirms the stability of the catalyst after cycling. The absence of peaks which could be assigned to Li_2O_2 was ascribed to the

insufficient crystallinity of the product, as indicated by TEM. To further confirm the presence of Li_2O_2 during discharge, XRD was performed on the cathode after a deep discharge of 5000 mAh/g (see Supporting Figure S10). The appearance of weak-intensity XRD peaks of Li_2O_2 after deep discharge is consistent with the previously reported study[40] on amorphous Li_2O_2 and the increase in its crystallinity with increasing the depth of discharge.

Moreover, to examine the Cu-THQ composition after battery cycling, XPS was carried out on the pristine and cycled cathode. Supporting Figure S11 presents the obtained Cu 2p spectra for the pristine cathode and after the 1st and 10th discharge. The Cu 2p XPS results suggest a shift from Cu^{2+} in the pristine cathode to Cu^{1+} species in the cycled cathodes.
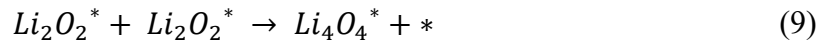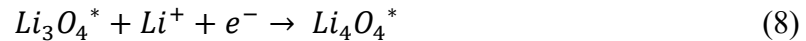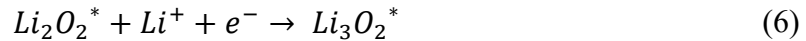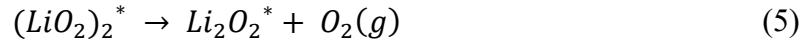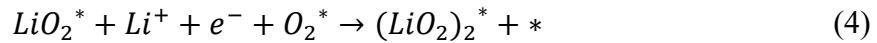
To evaluate the impedance of the Cu-THQ cathode, electrochemical impedance spectroscopy (EIS) was performed on the cathode and in the Li-O_2 battery cell as shown in Supporting Information S10. Furthermore, EIS was carried out on the Li‖Li symmetric coin cells to study the SEI layer on the anode. Figure 3a shows the Nyquist plots obtained for the Li‖Li symmetric cell at different cycling stages. The plots show semicircles at high frequency, representing the charge transfer resistance. Moving from the pristine stage to the 5th cycle, the charge transfer resistance increases from ~60 to ~63 ohms. The increase in the charge transfer resistance in the first few cycles can be attributed to the formation of an SEI layer[41]. After the 5th cycle and moving toward the higher cycles, the charge transfer resistance increases and finally stabilizes (~91.4 ohms) at the 15th cycle. The negligible difference in the charge transfer resistance values between the 10th and 15th cycles confirm the stabilization of the SEI layer. The model used to fit the EIS data is included in Supporting Information S10.

To investigate the composition of SEI layer, SEM- energy dispersive X-ray (EDX) spectroscopy was carried out on the Li anode surface (see Supporting Information S11). Figure 3b shows a top view SEM image of the anode after the 5th discharge. The SEM-EDX elemental analysis confirms the presence of indium on the Li surface, shown in purple in Figure 3c. Furthermore, XPS was performed to analyze the Li anode surface composition after the 5th cycle. Figure 3d shows the major peaks of In 3d region located at ~444.5 and ~452.1 eV. Two extra peaks are also observed at ~442.4 eV and ~449.5 eV. The observed four peaks suggest the formation of a SEI layer on the anode containing In and Li-In compounds[46,47].

To evaluate the long term and rate performance of the anode in our electrolyte, Li‖Li symmetric cell experiments were carried out. Figure 3e shows the galvanostatic cycling performance of Li‖Li

symmetric cell with a fixed stripping/plating capacity of 0.5 mAh/cm^2 at a current density of 0.5 mA/cm^2 using the 1M LiNO$_3$ and 0.1 M InBr$_3$ in TEGDME solvent. The battery exhibits a steady electrochemical performance of more than ~2000 hours with a low overpotential of ~0.2 V before the end of cycling. After approximately 2265 hours of continuous Li stripping and plating, a dendrite-induced short circuit is observed through voltage fluctuations. The rate performance of the symmetric cell was also investigated as shown in Figure 3f. A current density range of 0.1-2 mA/cm^2 was applied for a total of ~65 hours in this experiment. The Li‖Li symmetric cell shows a stable cycling under different current density rates with a low overpotential as high as ~0.5 V at a high current density of 2 mA/cm^2, which returns to the initial values upon shifting back to lower current densities.

DFT calculations were carried out to gain insight into the reaction mechanism of Li$_2$O$_2$ formation on the Cu-THQ cathode during discharging of a Li-O$_2$ battery. The formation can proceed via either Reaction (1-3) along with two electron transfer or the LiO$_2$ disproportionation reactions shown in (1-2, 4-5). The Reactions (6-9) describe the formation of Li$_2$O$_2$ dimer, (Li$_2$O$_2$)$_2$. The asterisk, *, represents the clean Cu-THQ surface, while the 'g' means the species is in gas phase.

$$O_2(g) + * \rightarrow O_2{}^* \tag{1}$$
$$O_2{}^* + Li^+ + e^- \rightarrow LiO_2{}^* \tag{2}$$
$$LiO_2{}^* + Li^+ + e^- \rightarrow Li_2O_2{}^* \tag{3}$$
$$LiO_2{}^* + Li^+ + e^- + O_2{}^* \rightarrow (LiO_2)_2{}^* + * \tag{4}$$
$$(LiO_2)_2{}^* \rightarrow Li_2O_2{}^* + O_2(g) \tag{5}$$
$$Li_2O_2{}^* + Li^+ + e^- \rightarrow Li_3O_2{}^* \tag{6}$$
$$Li_3O_2{}^* + O_2(g) \rightarrow Li_3O_4{}^* \tag{7}$$
$$Li_3O_4{}^* + Li^+ + e^- \rightarrow Li_4O_4{}^* \tag{8}$$
$$Li_2O_2{}^* + Li_2O_2{}^* \rightarrow Li_4O_4{}^* + * \tag{9}$$

The reaction free energies of Reactions (1-9) were calculated by defining the free energies of the Cu-THQ clean surface and gaseous O$_2$ as the reference. The free energy of Li ion and electron pair, $(Li^+ + e^-)$, is equivalent to that of bulk Li at potential U=0 by assuming the dissolution of metallic Li is in equilibrium[48]. The free energy profile describing Li$_2$O$_2$ formation on Cu-THQ is

displayed in Figure 4a. The O_2 adsorption from O_2 gas to the surface is exothermic with a free energy of -1.09 eV, shown as the first elementary step with the blue lines. The O_2 molecule binds to the Cu-THQ surface on one of Cu sites with a Cu-O bond length of 2.88 Å (see Figure 4b). The LiO_2 formation via the first Li ion and electron transfer (see Reaction (2)) is thermodynamically favorable with a reaction energy of -0.52 eV. A strong interaction between LiO_2 and Cu-THQ surface was observed. The Li-O bonds were formed via breaking the Cu-O bonds in the lattice, while the O atom in LiO_2 binds on the Cu site with a bond length of 1.93 Å, as shown in Figure 4c. The last step of the Li_2O_2 formation takes place from the second $Li^+ + e^-$ transfer to LiO_2 (Reaction 4 in blue lines) with a free energy of -0.69 eV. The Li_2O_2 adsorbed on Cu-THQ surface with a configuration bridging neighboring O site of Cu-THQ as depicted in Figure 4d. Another route for Li_2O_2 formation is the disproportionation reaction from LiO_2 dimer (Reactions 4-5, green lines in Figure 4a). Although the LiO_2 dimer formation as shown in Reaction 4 is exergonic with free energy of -1.06 eV and the LiO_2 dimer dissociated spontaneously to Li_2O_2 and O_2 upon the adsorption (see Supporting Figure S15 for the geometry), the disproportionation reaction of Reaction 5 (represented by the green line in Figure 4a), is endergonic by 0.38 eV on Cu-THQ.

One pathway for the Li_2O_2 dimer formation (Li_4O_4 or ($Li_2O_2)_2$) begins with the third electron transfer from Li_2O_2 to produce Li_3O_2 on Cu-THQ, as shown by Reaction 6 in blue lines in Figure 4a. The Li_3O_2 formation releases 0.69 eV in energy. Its geometry displays that two Li atoms of Li_3O_2 interact with the O site of Cu-THQ (see Figure 4e). Adding one more O_2 to Li_3O_2 gave Li_3O_4 with a free energy of -0.46 eV (see Reaction (7)). The Li_3O_4 interacts with both the Cu and O sites of Cu-THQ as displayed in Figure 4f. The Li_4O_4 formation by adding another $Li^+ + e^-$ (as described by Reaction 8) releases energy of 0.76 eV (see the blue lines of Figure 4a). The Li_4O_4 binds to the surface with Li atoms by bridging the O sites exposed at the edge of the mesohole of Cu-THQ, as depicted in Figure 4g. The second pathway for Li_4O_4 production is the Li_2O_2 dimerization via Reaction 9, as shown in red lines in Figure 4a. But this Li_2O_2 dimerization requires 0.38 eV in free energy to form Li_4O_4.

Finally, we have also examined the addition of four more Li_2O_2 units to the structure of Figure 4g, i.e. ($Li_2O_2)_n$ (n=2-6) cluster, growth on bilayer Cu-THQ. The optimized structure of bilayer Cu-THQ was displayed in Supporting Figure S16. The geometries of ($Li_2O_2)_n$ (n=2-6) adsorptions on bilayer Cu-THQ are depicted in Supporting Figure S17 and the negative formation energies

listed in Table S2 indicate that the formation of $(Li_2O_2)_n$ is energetically favorable in the pores of bilayer Cu-THQ.

The use of a two-dimensional copper-based conductive metal organic framework (c-MOF), copper tetrahydroxyquinone (Cu-THQ) in a Li-O_2 battery leads to a much better performance in terms of sustained low charge potentials than those batteries that have been reported based on non-conducting MOFs and MOF-derived cathodes[22,23,32,24–31]. The high active surface area and enhanced electronic conductivity of the Cu-THQ cathode paired with an electrolyte combination of $InBr_3$, $LiNO_3$, and TEGDME is found to enable a long cycle life (ranging from 100 to 300 cycles) with a stable and low charge overpotential (terminal charge potential <3.7 V) under high current density values of 1 and 2 A/g with capacities of 1000 and 2000 mAh/g. These results suggest the conductive framework helps to significantly improve the performance of MOF-based cathodes in Li-O_2 batteries.

The excellent performance of the Li-O_2 battery based on a conductive MOF is probably due to several factors. An important one is the characteristic of the discharge product. As shown from the TEM studies, the Li_2O_2 formed during discharge process has a nanocrystalline nature embedded in amorphous Li_2O_2. This type of product architecture has been previously shown to be effective in lowering the charge potential due to its enhanced electronic transport properties[49].

Operation at high current densities is enabled both by the c-MOF that provides good electronic conductivity at the active sites in the framework, and the conductive nature of Li_2O_2 product that can promote lower charge potentials[40,49–51].The DFT calculations we have carried out show that Li_2O_2 can form on the framework with the Cu being the most likely site for initial growth. The calculations were done on up to a hexamer of Li_2O_2 with favorable thermodynamics found. The addition of Li_2O_2 units to the dimer to form clusters as large as hexamer (Supporting Figure S17) do not occur on the c-MOF framework, but on already formed dimers attached to the framework. These additions are thermodynamically favorable (see formation energies in Table S2), and thus indicates that growth will continue to occur on the lithium peroxide surface away from the framework either in the pores or on the c-MOF surface.

Another factor in the excellent performance of the c-MOF is that the obtained Li_2O_2 structure, resulting from this cathode material, works in synergy with the $InBr_3$ additive in the electrolyte. The $InBr_3$ additive has previously been shown to give low charge potentials, although at lower rates and not as small polarization gaps[46,52]. $InBr_3$ forms an In-based SEI on the lithium anode

and also is a source of Br^- anion that acts as a redox mediator to reduce the charge potential and facilitate decomposition of the Li_2O_2[46,52]. These two functionalities contribute to the Li-O_2 battery performance reported here, i.e., a long cycle life (ranging from 100 to 300 cycles) with a stable and low charge overpotential (terminal charge potential <3.7 V). The $InBr_3$ works better in conjunction with the c-MOF than the previously studied MoS_2-based cathode for which the charge potential was ~3.9 V and the potential increased with number of cycles[52]. The better performance is because the conductivity of the Li_2O_2 structure allows the redox mediator to act directly on the Li_2O_2 surface instead of requiring oxidation (electron transfer) on MoS_2 edges and then transport through the electrolyte to the Li_2O_2 surface where it can catalyze decomposition of the Li_2O_2.

In summary, we have shown that incorporating electronic conductivity in a MOF results in a Li-O_2 battery with excellent performance. The conductive MOF with high active surface area promotes formation of nanocrystalline Li_2O_2 embedded in amorphous Li_2O_2 regions that are electronically conductive as opposed to crystalline Li_2O_2 that is an insulator. This property in combination with an $InBr_3$ electrolyte additive enables a battery that can operate with a high charge/discharge current density with a highly stable and significantly reduced charge overpotential, a well-retained Li_2O_2 discharge capacity and a long cycle life. The $InBr_3$ additive forms an In-based solid electrolyte interphase that protects the anode and is the source of the Br^- anion that acts as a redox mediator during charge for oxidation and Li_2O_2 decomposition. The latter process is facilitated by the conductive nature of the Li_2O_2 discharge product. DFT calculations of the growth of Li_2O_2 on the Cu-THQ framework indicated that its formation was thermodynamically favorable, and that the Cu was the growth site. These findings open a new direction in achieving high-rate Li-air batteries with enhanced energy efficiency.
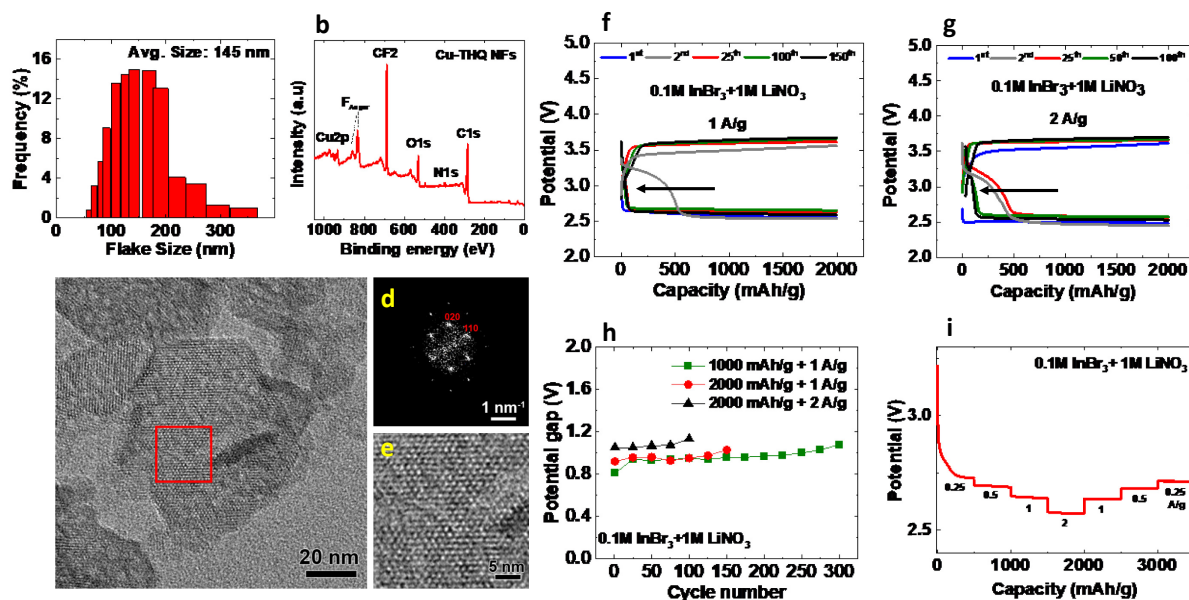
Figure 1- Cu-THQ NFs characterization and performance of a Li-O₂ battery system using Cu-THQ NFs, 1M LiNO₃, 0.1 M InBr₃ and TEGDME solvent (a) Lateral size distribution of Cu-THQ NFs. **(b)** XPS survey spectrum of Cu-THQ NFs coated on GDE. **(c)** TEM image of Cu-THQ NFs along [001] direction. **(d)** Fourier transforms of the image. **(e)** HRTEM image in the red box in (c), showing the open pores along *c*-axis. The charge-discharge voltage profiles of the battery with **(f)** 1 A/g current density rate. **(g)** 2 A/g current density rate. **(h)** Charge-discharge potential gap of the battery under different rate and limiting capacity conditions. **(i)** Rate capability of a battery under different rates. Inset shows the galvanostatic discharge profile for Cu-THQ with 1 A/g rate and cut-off potential of 2.20 V.
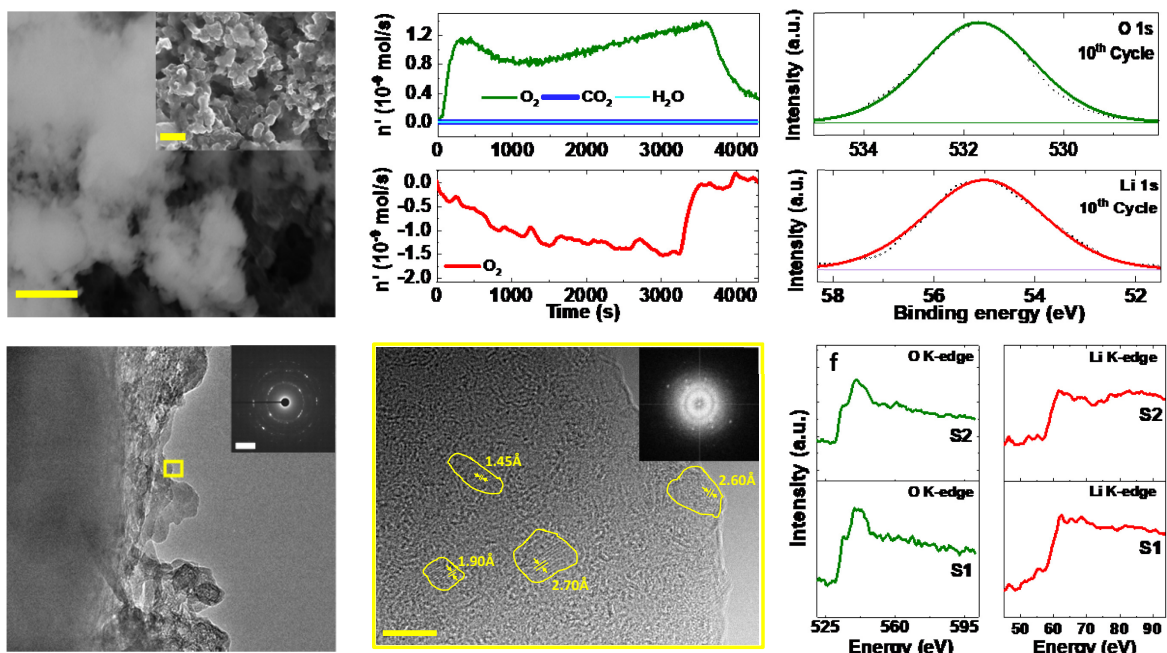
Figure 2 - Characterization of Cu-THQ cathode in the Li-O₂ battery containing 1M LiNO₃, 0.1 M InBr₃ and TEGDME solvent run at 2 A/g (a) SEM image of cathode after the 10th discharge. The inset is the image of cathode after the 10th charge. The scale bar in the inset is 200 nm. **(b)** DEMS results during the discharge and charge processes **(c)** XPS results of the cathode after the 10th discharge including O 1s and Li 1s spectra. **(d)** TEM image of the cathode after the 10th discharge. Diffraction pattern of the Cu-THQ catalyst is shown in the inset (scale bar is 5 nm⁻¹**). (e)** High resolution TEM image of the Li₂O₂ product after the 10th discharge. The corresponding fast Fourier transform (FFT) pattern is shown in the inset (see Supporting Figure S7a and mp-841, Materials Project for Li₂O₂ indexing). Scale bar in the inset is 5 nm⁻¹. **(f)** EELS data showing the O K- and Li K-edges at two different locations, which are labeled as 'S1' and 'S2', within a Cu-THQ flake after the 10th discharge. The TEM micrograph of this sample and the regions from which the EELS data are acquired can be found in Supporting Figure S7b.
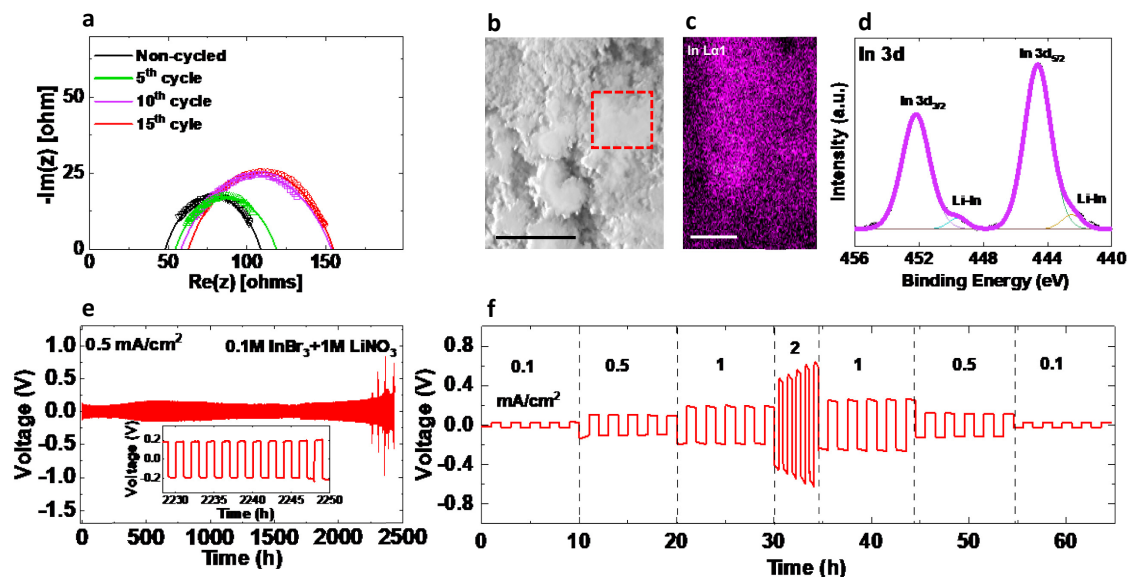
12

Figure 3 - Characterization and performance of the Li∥Li symmetric cells containing 1M LiNO₃, 0.1 M InBr₃ and TEGDME solvent. (a) EIS results of Li∥Li symmetric cell after 5, 10 and 15 cycles compared to non-cycled anode. **(b)** Top-view SEM image of the anode after the 5th cycle (Scale bar is 5 μm). **(c)** SEM-EDX composition mapping of anode for detected indium element (Scale bar is 500 nm) **(d)** Anode XPS result obtained for In 3d region after the 5th cycle. **(e)** Long-term cycling of Li∥Li symmetrical cell with current density of 0.5 mA/cm² and fixed capacity of capacity of 0.5 mAh/cm². The inset presents the details of the voltage vs. time profile towards the end of cycling. **(f)** Rate performance of Li∥Li symmetrical cell under different current densities.
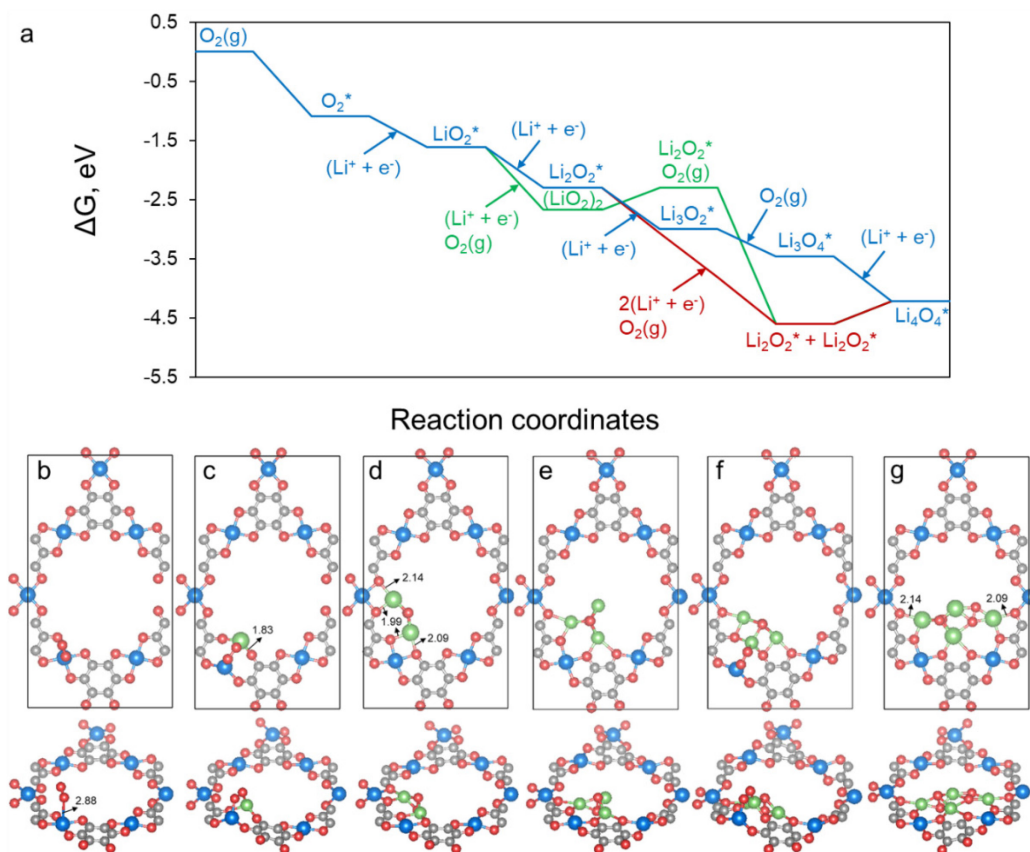
13

Figure 4 – Density Functional Theory Calculation Results. (a) The free energies for Li_2O_2 formation on Cu-THQ at 0 V. The blue lines represent Reactions (1-3, 6-8), the green lines describe the Reactions (4-5) and the red lines describe Reaction (9). The adsorption configuration with top-view (upper panel) and side-view (bottom panel) are shown as follows: **(b)** O_2, **(c)** LiO_2, **(d)** Li_2O_2, **(e)** Li_3O_2, **(f)** Li_3O_4 and **(g)** Li_4O_4 on Cu-THQ. The Cu, C, O and Li are in blue, grey, red and green, respectively. The periodic boundaries are represented in black lines. The selective bond lengths are labeled in Å.

Experimental Section

Cathode Preparation: Cu-THQ NFs were synthesized using a liquid-phase exfoliation method. 30 mg of the Cu-THQ powder was dispersed in 12 mL of IPA. An ultra-sonication (Vibra Cell Sonics 130 W) was used for 4 hours followed by centrifugation for 60 minutes at 2000 rpm to obtain the NFs. For cathode preparation, 100 mg of Cu-THQ NFs was coated on 1 cm^2 of GDE (Sigracet 25 BC, purchased from FuelCellsEtc).

DLS Experiments: A Malvern Zetasizer Nano ZSP was used to measure the lateral size of Cu-THQ NFs dispersed in IPA at 25 °C. The instrument operates with a 10 mW semiconductor laser with 633 nm emissions.

TEM Experiments: Samples for TEM observation were diluted in IPA. A droplet of the suspension was transferred onto a carbon-coated copper grid. High-angle annular dark-field (HAADF) STEM imaging and EDS mapping were performed on a JEOL JEM2100 microscope, and operated at 200 kV (Cs 1.0 mm, point resolution 0.23 nm). TEM images were recorded with a Gatan Ultrascan CCD camera (resolution 2048 x 2048 pixels).

The discharged cathodes were analyzed using the TEM; JEOL JEM-ARM200CF operating at 80 kV. The TEM samples were prepared by sonicating the discharged cathode for 15 minutes in acetonitrile. The resulting solution was then drop cast onto holey carbon coated copper TEM grids (200 mesh, SPI Supplies). EELS was performed using a probe-corrected scanning transmission electron microscope (JEOL JEM-ARM200CF) equipped with a 200 kV cold-field emission source.

XPS Experiments: A Thermo Scientific ESCALAB 250Xi instrument was used to carry out XPS experiments. Thermo Avantage software was used to analyze and process each element's data. All spectra were calibrated based on C-C binding energy at 284.8 eV.

Li-O$_2$ Battery Experiments: Custom-made Swagelok battery setups were assembled in an argon-filled glovebox. The Cu-THQ coated GDE was used as the cathode. 40 µL of the electrolyte was added on a glass microfiber filter as a separator. Dry air was purged in the batteries for approximately 20 minutes and the batteries were left at rest for at least 1 hour before operation.

Li‖Li Symmetric Battery Experiments: Coin cell symmetric battery cells were assembled in an argon filled glovebox. Two bare Li chips were used in the symmetric battery separated with the Celgard 3401 membrane.

DEMS Experiments: Real time analysis of the gas products was carried out using DEMS (purchased from Hiden Analytical) after discharge and charge process of Li-O$_2$ battery. A calibration was carried out for oxygen by using 2%, 5%, 10% and 20% of O$_2$ in argon. For further details of DEMS experiments see Supporting Information S6.

XRD Experiment: Powder XRD was performed for the discharged cathode on a Bruker D8 Advance (40 kV, 40 mA) using a Cu Kα (λavg = 1.5418 Å).

DFT Calculations: For details of DFT calculations see Supporting Information S12.

Author contributions

L.M. synthesized the c-MOF NFs and obtained the DLS results. L.M. carried out the battery experiments. A.A. performed the DEMS experiments. L.M. performed the XPS experiments. Z.H. performed SEM and SEM/EDX. L.M. and S.R. performed EIS. A.S.K. supervised the electrochemical and characterization experiments. S.S. and A.S. carried out the TEM and EELS for the cathode. Zh.H. performed the HRTEM experiment of the Cu-THQ NFs. K.K. and J.C. performed the XRD of the cathode. N.S., P.Z. and L.C. carried out the computational studies (DFT).

References

[1]   M. Balaish, J. Jung, I. Kim, Y. Ein-Eli, *Adv. Funct. Mater.* **2020**, *30*, 1808303.

[2]   M. Asadi, B. Sayahpour, P. Abbasi, A. T. Ngo, K. Karis, J. R. Jokisaari, C. Liu, B. Narayanan, M. Gerard, P. Yasaei, X. Hu, A. Mukherjee, K. C. Lau, R. S. Assary, F. Khalili-Araghi, R. F. Klie, L. A. Curtiss, A. Salehi-Khojin, *Nature* **2018**, *555*, 502.

[3]   Y. Chen, S. A. Freunberger, Z. Peng, O. Fontaine, P. G. Bruce, *Nat. Chem.* **2013**, *5*, 489.

[4]   H.-D. Lim, B. Lee, Y. Zheng, J. Hong, J. Kim, H. Gwon, Y. Ko, M. Lee, K. Cho, K. Kang, *Nat. Energy* **2016**, *1*, 16066.

[5]   A. C. Luntz, B. D. McCloskey, *Chem. Rev.* **2014**, *114*, 11721.

[6]   P. G. Bruce, S. a. Freunberger, L. J. Hardwick, J.-M. Tarascon, *Nat. Mater.* **2011**, *11*, 172.

[7]   L. Majidi, P. Yasaei, R. E. Warburton, S. Fuladi, J. Cavin, X. Hu, Z. Hemmat, S. B. Cho, P. Abbasi, M. Vörös, L. Cheng, B. Sayahpour, I. L. Bolotin, P. Zapol, J. Greeley, R. F. Klie, R. Mishra, F. Khalili-Araghi, L. A. Curtiss, A. Salehi-Khojin, *Adv. Mater.* **2019**, *31*, 1804453.

[8]   L. Majidi, Z. Hemmat, R. E. Warburton, K. Kumar, A. Ahmadiparidari, L. Hong, J. Guo, P. Zapol, R. F. Klie, J. Cabana, J. Greeley, L. A. Curtiss, A. Salehi-Khojin, *Chem. Mater.* **2020**, *32*, 2764.

[9]   F. Wu, Y. Yu, *Joule* **2018**, *2*, 815.

[10]   J. Xie, Q. Dong, I. Madden, X. Yao, Q. Cheng, P. Dornath, W. Fan, D. Wang, *Nano Lett.* **2015**, *15*, 8371.

[11]   Z. Liang, R. Zhao, T. Qiu, R. Zou, Q. Xu, *EnergyChem* **2019**, *1*, 100001.

[12]   X. Li, X. Yang, H. Xue, H. Pang, Q. Xu, *EnergyChem* **2020**, *2*, 100027.

[13]   K.-B. Wang, Q. Xun, Q. Zhang, *EnergyChem* **2020**, *2*, 100025.

[14]   Y. Zhao, Z. Song, X. Li, Q. Sun, N. Cheng, S. Lawes, X. Sun, *Energy Storage Mater.* **2016**, *2*, 35.

[15]   R. Zhao, Z. Liang, R. Zou, Q. Xu, *Joule* **2018**, *2*, 2235.

[16]   T. Mehtab, G. Yasin, M. Arif, M. Shakeel, R. M. Korai, M. Nadeem, N. Muhammad, X. Lu, *J. Energy Storage* **2019**, *21*, 632.

[17]   H. Meng, Y. Han, C. Zhou, Q. Jiang, X. Shi, C. Zhan, R. Zhang, *Small Methods* **2020**, *4*, 2000396.

[18]   D. Sheberla, J. C. Bachman, J. S. Elias, C. Sun, Y. Shao-Horn, M. Dincă, *Nat. Mater.*

2017, *16*, 220.

[19]   X. Deng, J. Y. Hu, J. Luo, W. M. Liao, J. He, *Conductive Metal–Organic Frameworks:*
Mechanisms, Design Strategies and Recent Advances, Springer International Publishing,
2020.

[20]   M. Ko, L. Mendecki, K. A. Mirica, *Chem. Commun.* **2018**, *54*, 7873.

[21]   W.-H. Li, W.-H. Deng, G.-E. Wang, G. Xu, *EnergyChem* **2020**, *2*, 100029.

[22]   S. zhi Yu, S. hua Luo, Y. Zhan, H. bo Huang, Q. Wang, Y. hui Zhang, Y. guo Liu, A. in
Hao, *J. Power Sources* **2020**, *453*, 227899.

[23]   J. Li, Y. Deng, L. Leng, M. Liu, L. Huang, X. Tian, H. Song, X. Lu, S. Liao, *J. Power*
Sources **2020**, *450*, 227725.

[24]   D. Liu, X. Zhang, Y. J. Wang, S. Song, L. Cui, H. Fan, X. Qiao, B. Fang, *Nanoscale* **2020**,
12, 9524.

[25]   Y. Dou, R. Lian, Y. Zhang, Y. Zhao, G. Chen, Y. Wei, Z. Peng, *J. Mater. Chem. A* **2018**,
6, 8595.

[26]   S. Y. Zhen, H. T. Wu, Y. Wang, N. Li, H. Sen Chen, W. L. Song, Z. H. Wang, W. Sun, K.
N. Sun, *RSC Adv.* **2019**, *9*, 16288.

[27]   D. Wu, Z. Guo, X. Yin, Q. Pang, B. Tu, L. Zhang, Y. G. Wang, Q. Li, *Adv. Mater.* **2014**,
26, 3258.

[28]   Q. Li, P. Xu, W. Gao, S. Ma, G. Zhang, R. Cao, J. Cho, H. L. Wang, G. Wu, *Adv. Mater.*
2014, *26*, 1378.

[29]   M. J. Song, I. T. Kim, Y. B. Kim, J. Kim, M. W. Shin, *Electrochim. Acta* **2017**, *230*, 73.

[30]   Y. Zhao, L. Ding, X. Wang, X. Yang, J. He, B. Yang, B. Wang, D. Zhang, Z. Li, *J. Alloys*
Compd. **2021**, *861*, 157945.

[31]   A. Chatterjee, S. W. Or, *Electrochim. Acta* **2020**, *338*, 135809.

[32]   M. Yuan, R. Wang, W. Fu, L. Lin, Z. Sun, X. Long, S. Zhang, C. Nan, G. Sun, H. Li, S.
Ma, *ACS Appl. Mater. Interfaces* **2019**, *11*, 11403.

[33]   J. Park, A. C. Hinckley, Z. Huang, D. Feng, A. A. Yakovenko, M. Lee, S. Chen, X. Zou,
Z. Bao, *J. Am. Chem. Soc.* **2018**, *140*, 14533.

[34]   L. Majidi, A. Ahmadiparidari, N. Shan, S. N. Misal, K. Kumar, Z. Huang, S. Rastegar, Z.
Hemmat, X. Zou, P. Zapol, J. Cabana, L. A. Curtiss, A. Salehi-Khojin, *Adv. Mater.* **2021**,
2004393.

[35] S. Yu, X. Li, S. Liu, J. Hao, Z. Shao, B. Yi, *RSC Adv.* **2014**, *4*, 3852.

[36] X. Xin, K. Ito, Y. Kubo, *ACS Appl. Mater. Interfaces* **2017**, *9*, 25976.

[37] W. J. Kwak, D. Hirshberg, D. Sharon, M. Afri, A. A. Frimer, H. G. Jung, D. Aurbach, Y. K. Sun, *Energy Environ. Sci.* **2016**, *9*, 2334.

[38] K. N. Wood, G. Teeter, *ACS Appl. Energy Mater.* **2018**, *1*, 4493.

[39] M. Asadi, B. Sayahpour, P. Abbasi, A. T. Ngo, K. Karis, J. R. Jokisaari, C. Liu, B. Narayanan, M. Gerard, P. Yasaei, X. Hu, A. Mukherjee, K. C. Lau, R. S. Assary, F. Khalili-Araghi, R. F. Klie, L. A. Curtiss, A. Salehi-Khojin, *Nature* **2018**, *555*, 502.

[40] H. G. Jung, H. S. Kim, J. B. Park, I. H. Oh, J. Hassoun, C. S. Yoon, B. Scrosati, Y. K. Sun, *Nano Lett.* **2012**, *12*, 4333.

[41] W. Wang, Z. Favors, C. Li, C. Liu, R. Ye, C. Fu, K. Bozhilov, J. Guo, M. Ozkan, C. S. Ozkan, *Sci. Rep.* **2017**, *7*, 44838.

[42] Z. Xu, J. Wang, J. Yang, X. Miao, R. Chen, J. Qian, R. Miao, *Angew. Chemie Int. Ed.* **2016**, *55*, 10372.

[43] G. Bieker, M. Winter, P. Bieker, *Phys. Chem. Chem. Phys.* **2015**, *17*, 8670.

[44] Y. Cui, S. Liu, B. Liu, D. Wang, Y. Zhong, X. Zhang, X. Wang, X. Xia, C. Gu, J. Tu, *Front. Chem.* **2020**, *7*, DOI 10.3389/fchem.2019.00952.

[45] E. Markevich, G. Salitra, F. Chesneau, M. Schmidt, D. Aurbach, *ACS Energy Lett.* **2017**, *2*, 1321.

[46] J. Liu, T. Wu, S. Zhang, D. Li, Y. Wang, H. Xie, J. Yang, G. Sun, *J. Power Sources* **2019**, *439*, 227095.

[47] X. Liang, Q. Pang, I. R. Kochetkov, M. S. Sempere, H. Huang, X. Sun, L. F. Nazar, *Nat. Energy* **2017**, *2*, 1.

[48] J. S. Hummelshøj, J. Blomqvist, S. Datta, T. Vegge, J. Rossmeisl, K. S. Thygesen, A. C. Luntz, K. W. Jacobsen, J. K. Nørskov, *J. Chem. Phys.* **2010**, *132*, 071101.

[49] J. Lu, Y. Lei, K. C. Lau, X. Luo, P. Du, J. Wen, R. S. Assary, U. Das, D. J. Miller, J. W. Elam, H. M. Albishri, D. A. El-Hady, Y.-K. Sun, L. A. Curtiss, K. Amine, *Nat. Commun.* **2013**, *4*, 2383.

[50] F. Tian, M. D. Radin, D. J. Siegel, *Chem. Mater.* **2014**, *26*, 2952.

[51] Y. Zhang, Q. Cui, X. Zhang, W. C. McKee, Y. Xu, S. Ling, H. Li, G. Zhong, Y. Yang, Z. Peng, *Angew. Chemie - Int. Ed.* **2016**, *55*, 10717.

[52]   S. Rastegar, Z. Hemmat, C. Zhang, S. Plunkett, J. Wen, N. Dandu, T. Rojas, L. Majidi, S. N. Misal, A. T. Ngo, L. A. Curtiss, A. Salehi-Khojin, *ACS Appl. Mater. Interfaces* **2021**, acsami.0c15200.